Journal of Nondestructive Evaluation (2025) 44:99
https://doi.org/10.1007/s10921-025-01240-7

Enhancing Computed Tomography-Based Pore Mesh Models Through Matching with Microscope Cross-Section Images

Sebastian Mansky[1] · **Malte Becker**[1] · **Dirk Herzog**[1,2] · **Ingomar Kelbassa**[1,2]

Received: 14 May 2025 / Accepted: 7 July 2025

Abstract

X-Ray Computed Tomography (CT) is a widely adopted tool in the non-destructive quality assurance of additive manufacturing (AM). Porosity in AM can be assessed via CT without compromising the integrity of the part and without reliance on witness specimen. Reliable pore criticality analysis, essential for AM fatigue assessments, hinges on precise determination of pore dimensions. This work investigates CT data by comparing the pore sizes and shapes from two different data sources (CT and metallography), originating from the same samples. The comparison indicates a pore size underestimation in the CT data by an average of 20%. A subsequent rescaling and smoothing workflow on the CT pore data compensates this underestimation. This workflow reduces the mean pore size deviations between both data sources by up to 50% compared to the original data, allowing a more accurate pore assessment. Additionally the smoothing process reduces errors introduced by the CT reconstruction, lowering the average and scatter in mean curvature between pores. The rescaled and smoothed pores serve as an improved starting point for investigations regarding the effect of porosity on fatigue in AM.

Keywords Additive manufacturing · X-ray Computed Tomography · Smoothing · Microscope images · Cross-sections

1 Introduction

Porosity in additive manufacturing (AM) is impacting the mechanical performance and reliability of manufactured components [1]. Despite significant advancements in process optimization aimed at minimizing porosity, the complete elimination of voids in AM parts remains improbable in the foreseeable future [2]. Consequently, accurate detection and characterization of porosity are essential for AM quality assurance. The presence of pores can significantly reduce the fatigue life of AM parts. Predictive models evaluating the impact of porosity on fatigue typically rely on specific pore parameters, such as size and shape, to estimate reductions in material performance [3, 4]. Other models directly use the three-dimensional pore data generated by CT as an input for finite element based fatigue simulations either via external mesh generation [5–7] or image based meshing [8, 9]. Therefore, precise measurement of these pore characteristics is imperative. Non-destructive testing (NDT) methods, particularly X-ray computed tomography (CT), and destructive testing on witness specimens are commonly employed to assess pore dimensions or to generate a pore size distribution model. CT imaging offers a three-dimensional reconstruction of AM parts, enabling the detection of porosity based on density contrasts between voids and the surrounding material. Laboratory-based CT systems typically achieve voxel sizes around 10 µm, while high-energy beams like synchrotron radiation can attain sub-micron resolutions. However, industry-standard CT scans use larger voxel sizes to reduce costs and because the inspected parts are larger. This may result in inadequate modelling of pores close to the resolution limit and in the inability to detect pores below a certain size. Porosity below three times the voxel size is challenging to distinguish from image noise, potentially leading to under-representation of critical voids [10].

Error estimation in CT metrology is an ongoing research topic. A review of Villarraga-Gómez et al. [11] describes different empirical approaches to uncertainty analysis in CT measurements, concluding that the measurement accuracy is dependent on a multitude of CT and part specific parameters.

✉ Sebastian Mansky
sebastian.mansky@iapt.fraunhofer.de

[1] Fraunhofer Research Institution for Additive Manufacturing Technologies IAPT, Am Schleusengraben 14, 21029 Hamburg, Germany

[2] Institute for Industrialization of Smart Materials, TU Hamburg, 21073 Hamburg, Germany

A comparison with coordinate measure machines as ground truth to reduce measurement uncertainty is not always useful or possible. Holgado et al. [12] compare CT data with optical reference measurements and evaluate the CT measurement uncertainty. Carmignato et al. [13] test the dimensional accuracy of 15 CT systems with spheres of different diameters (140 to 400 µm). They report an increase in size error as the sphere diameter decreases, as well as an increase in size error as the scan resolution increases, which was also detected in this article. The CT scan parameters also influence the measurement accuracy [14], which are not considered in this work. Other authors also detect deviations between CT data compared to microscopic image measurement. Schild et al. [15] detect under- and overestimations of pore sizes, with outliers and large discrepancies for two different CT scan parameter sets. As discussed in [15], multiple error sources in the CT scan and the metallographic preparation could influence the results. Lifton and Liu [16] develop and use an adaptive thresholding algorithm instead of the common Otsu algorithm [17]. They compare porosity measurements via CT and Archimedes principle and reported decreased porosity deviations between both measurement principles with their algorithm.

This study aims to evaluate the differences between CT-based and metallographic imaging techniques in porosity characterization. By comparing pore data obtained from both CT scans and metallographic optical microscopy of the same AM specimens, the accuracy and reliability of CT scans is evaluated. The specimens produced by Laser Powder Bed Fusion (PBF-LB) were processed with varying parameter sets to induce specific types of porosity. After manufacturing, the samples underwent CT scanning followed by metallographic preparation and microscopic imaging. A matching process between the two datasets allows for a comparison of pore size and shape. The study aims to imitate elements of an industrial AM production process. The manufacturing of metallographic witness specimen, as well as the CT imaging for high value parts is common in the industry as continuous quality assurance.

2 Methodology

This study compares pores derived from two distinct data sources: metallographic optical images (MS) and reconstructed pores from CT scans. To ensure consistency, the same object was analysed, guaranteeing that the pores are identical while the data sources vary. A flowchart depicting the data acquisition process is shown in Fig. 1.

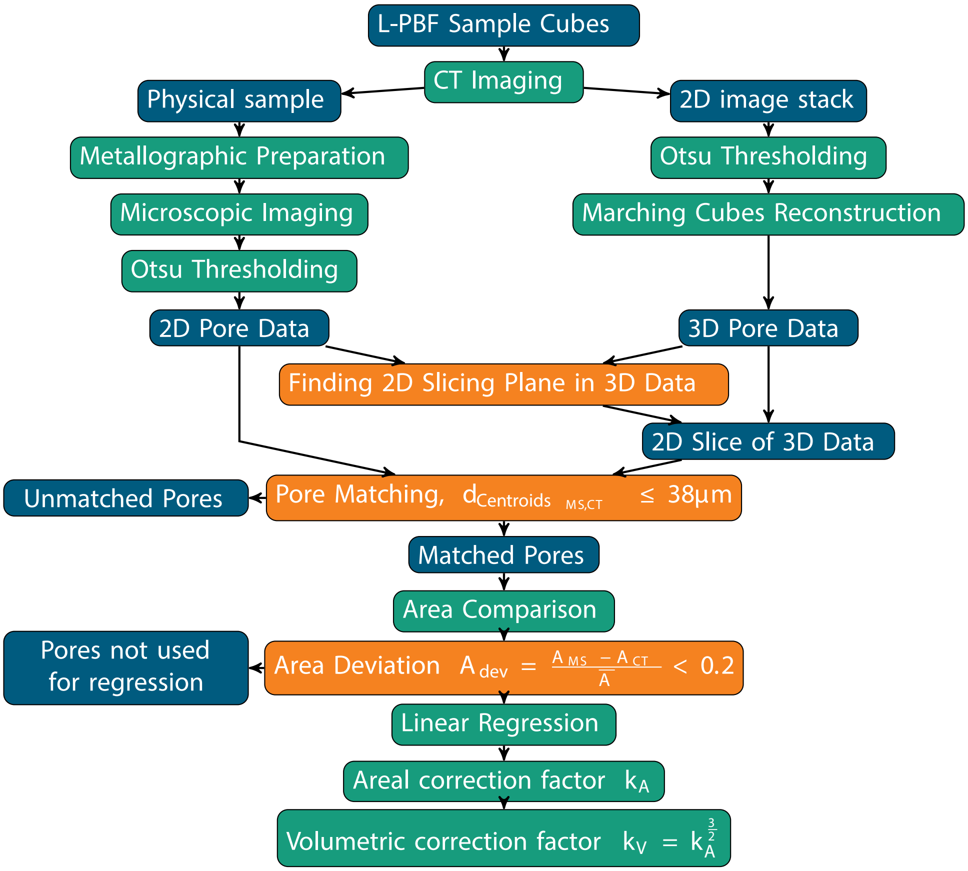

Fig. 1 Pore data processing workflow for metallography and CT, estimation of correction factor after pore matching

Table 1 Relevant process parameters used for the production of the analysed samples

Parameter Set	Laser Power [W]	Scan Speed [mm/s]	Hatch Distance [mm]	Layer Thickness [mm]	Energy Density [J/mm^3]
Standard (Std)	175	1500	0.10	0.02	58.33
Gas Porosity (GP)	175	1500	0.08	0.02	72.92
Lack-of-Fusion (LoF)	150	1500	0.09	0.04	27.78

The energy density was altered compared to the optimal state to induce specific types of pores in the material

2.1 Data Acquisition

Three samples of additive manufactured AlSi10Mg were produced on a Trumpf TruPrint1000 (TRUMPF, Ditzingen, Germany). The samples are of cuboid shape with a conic end to ease separation from the build platform, with a length and width of 10 mm and a height in build direction of 15 mm. The two most common types of internal defects in AM, gas porosity and Lack-of-Fusion defects, were induced into the material by altering the energy density during production. Two parameter sets were changed to induce specific types of porosity into the material, while the third sample was produced with standard parameters to compare the induced porosities to common production porosities. The adjusted parameters of the parameter sets are shown in Table 1. The altered parameters increase the occurrence of specific defects, but are not excluding the occurrence of other defects, e.g. the parameter set 'LoF' produces mostly Lack-of-Fusion defects, but gas porosity can still occur within the material and can subsequently be detected via CT scanning. Other types of internal defects can be forced within an AM process, but the two selected defect types are the most common [1]. The hatching pattern angle was not changed after each layer, which produces pores in distinct columns parallel to the building direction (see Fig. 2). These columns help in matching the porosity detected by both data sources. After manufacturing, all three specimen were CT scanned on a V|Tome|x M (Waygate Technologies, Hürth, Germany). The samples were scanned at a resolution of 10 µm. The resulting 2D image stacks (between 1933 and 1994 images) were binarized via Otsu's thresholding method [17] and reconstructed into 3D models using the Marching-Cubes algorithm [18, 19].

After the non-destructive data acquisition the samples were embedded in resin in a CitoPress (Struers, Copenhagen, Denmark), then ground and polished on a Tegramin 30 (Struers, Copenhagen, Denmark) to achieve surfaces suitable for imaging. The abrasive metallographic preparation process is detailed in Table 2.

High-resolution images were captured using a VHX 5000 (Keyence, Osaka, Japan) optical microscope. Figure 2 shows the images of the cut sections of the samples with different processing parameters. The different level of porosity can be clearly seen, also notable are the different pore sizes comparing the "GP" parameters and the "LoF" parameters (see Fig. 2b and c). The microscopic image was thresholded using Otsu's method [17] to differentiate the pores from the surrounding material. Subsequently, the pores were labeled using the Python library scikit-image [19], allowing for individual pore identification. Some shape distortion might arise during sectioning and polishing. The measured pore size from metallography might not perfectly represent the original pore.

2.2 Image Correlation

The metallographic image was imported into the 3D CT data to identify the corresponding slicing plane within the 3D reconstruction. The 3D model was sectioned along this slicing plane, and the resulting cut surface was exported for further analysis. A Nearest Neighbor search [20] was performed to match pores between the metallographic images and the CT cut surfaces, with a threshold set for maximum distance to prevent false matches. The threshold was set to eight pixels, corresponding to a circle with a radius of 38 µm centered on each CT pore's centroid. This threshold allows

Table 2 Metallographic preparation process for the AlSi10Mg samples

Grinding Foil	Lubrication Suspension	Revolutions [1/min] Foil	Specimen	Force [N]	Time [min]
SiC Foil #320	Water	320	150	20	10
SiC Foil #2000	Water	300	150	20	2
MD-Largo	DiaDuo 9µm	120	80	20	8
MD-Mol	DiaDuo 3µm	80	100	20	4
MD-Nap	DiaDuo 1µm	120	80	20	3.5

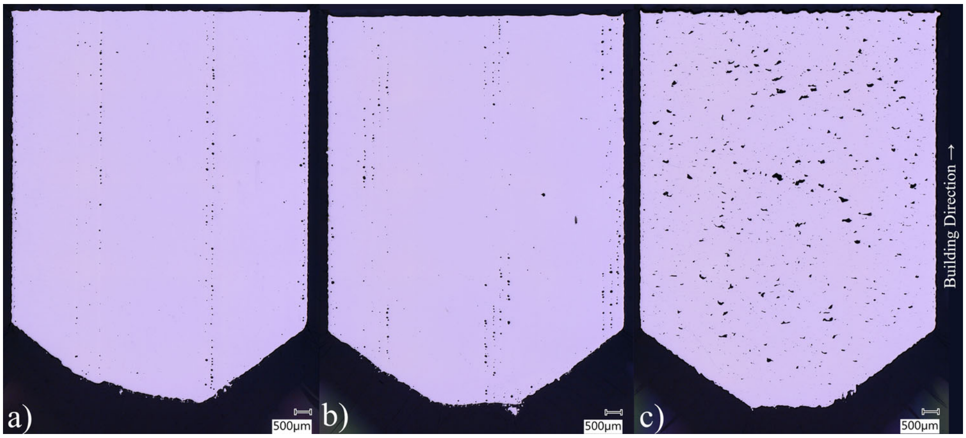

Fig. 2 Microscopic images of the samples produced with parameter sets “Std" (a), “GP" (b) and “LoF" (c) after metallographic preparation

a matching of most of the pores detected via CT (see Table 3), while excluding spurious defects introduced by metallographic sample preparation. A match between CT and MS pores was declared if the centroid of a CT pore coincided with an MS pore either at the same location or within the specified eight-pixel radius. Figure 3 shows the results of the matching process between both surface datasets. Figure 3b shows a section of the surface, indicating the good match between pores for pores larger than 30 µm. The centroids of both datasets don’t match perfectly, due to a constant offset. This offset does not influence the results of the area comparison, since it is below 8 pixels. The contour matches were further processed to calculate and compare their respective cut surface area.

2.3 Image Data Comparison

Differences between the two data sources for the matched pores were analysed, focusing on discrepancies in the calculated cut section area. Systematic deviations in pore area measurements between CT-derived pores and metallographic data were identified as shown in Fig. 4.

For all parameter sets, on average the pore area detected by CT is lower than for the same pores detected by metallography. To estimate the global difference, a linear regression was conducted using pores with less than a 20 % area deviation between the two data sources. The area deviation constraint ensures that the regression is not influenced by outliers. Only a subsection of pores is used for the calculation of the cor-

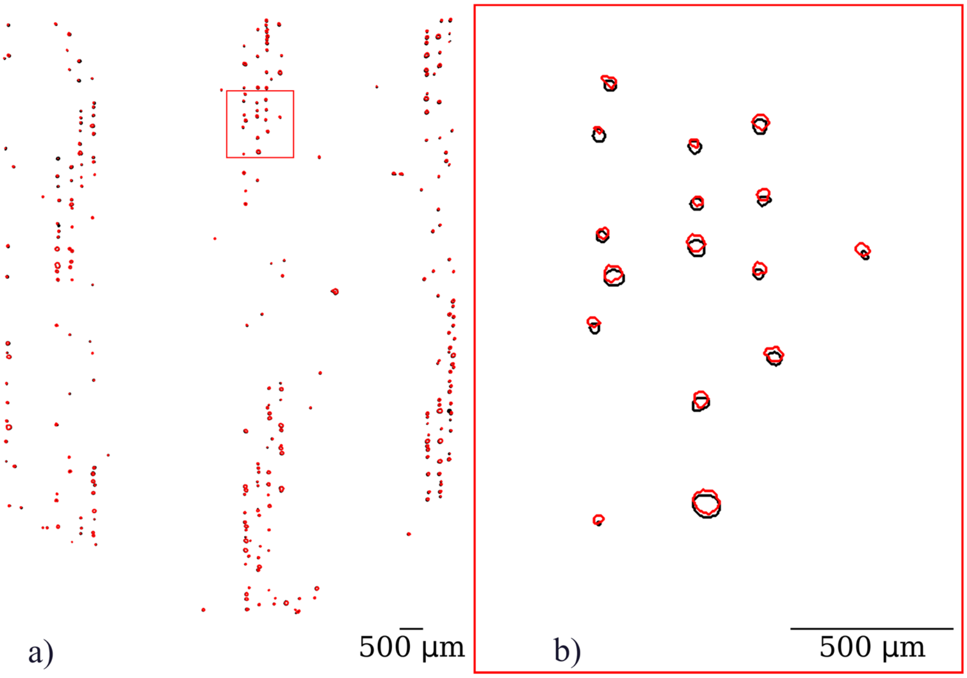

Fig. 3 Surface matching results for parameter set “GP". Black represents metallographic data, while red represents CT data. Pores smaller than the CT resolution limit (10 µm) were only detectable through metallographic imaging. b) shows an enlarged section of the matched data, similarities between both data sources are visible

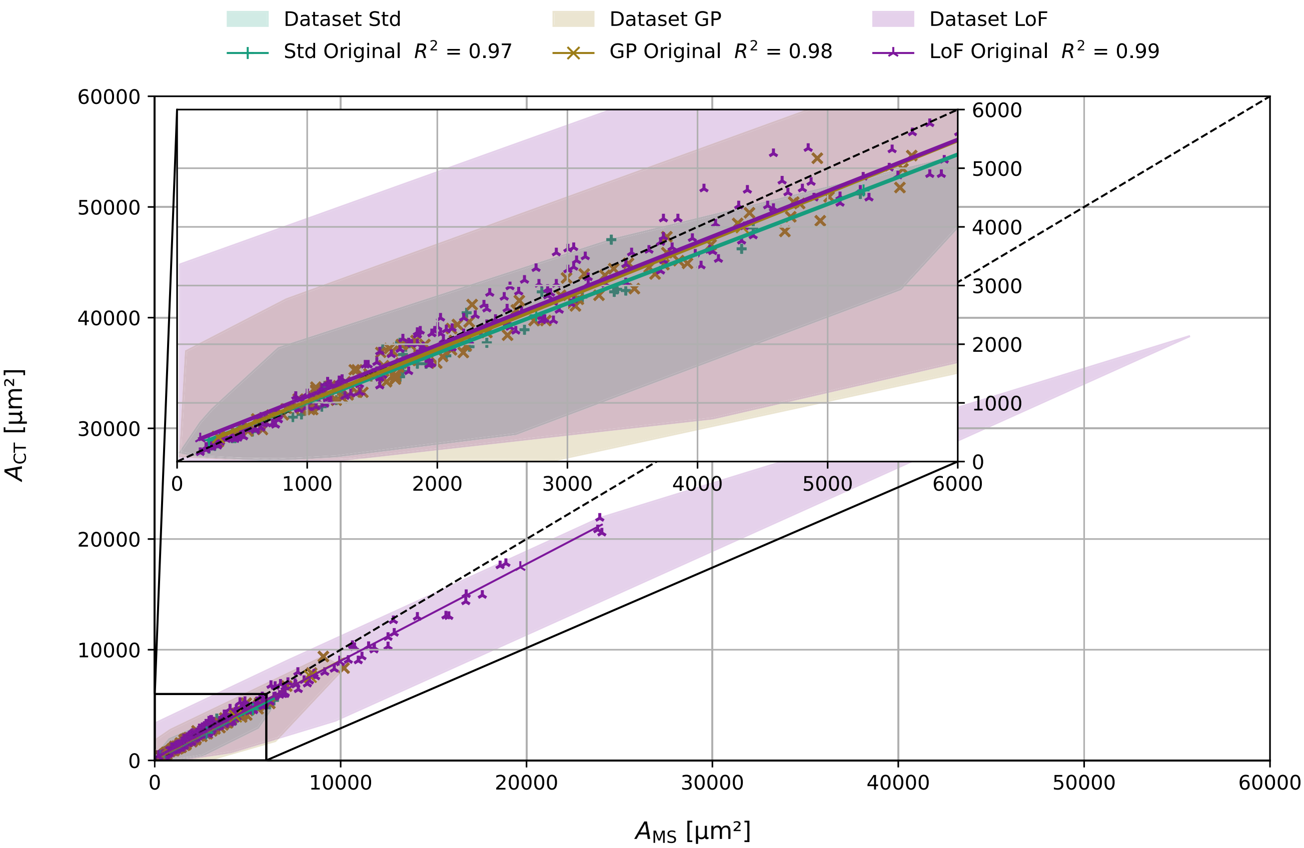

Fig. 4 Plot of the area difference between the metallographic and computed tomography data source for all parameter sets. The dashed line indicates same areas measured by the CT and MS at the cut section. The enlarged section shows smaller pores (cut section up to 6000 μm^2) present in the parameter set “Std" and “GP", the coloured areas depict all matched pores in the parameter sets, while the scatterpoints depict the dataset of each parameter set used for the linear regression

rection factors, mainly due to the large scatter in cut section areas measured from both data sources. The coloured areas in Fig. 4 show the complete pore dataset for all three parameter sets, while the pores used for the regression are displayed as coloured markers. The linear regression shows an underestimation of the pore area by the CT data source for all parameter sets.

To quantify the deviation, a global areal correction factor k_A, based on the linear regression was used for each parameter set. The area-based correction factor was then converted into a volume-based factor k_V, based on the assumption that the pores are spherical or approximately spherical. For pores from the parameter sets “Std" and “GP", the roundness $R = P^2/(4\pi A)$ with the pore perimeter P and the pore area A is equal or less than 1.2 for more than 93 % of the pores. This is only true for 44 % of the pores from the parameter set “LoF". The assumption of circularity and subsequent sphericity seems only valid for the parameter sets “Opt" and “GP".

Further processing is also done on the parameter set “LoF", to see the effect of the rescaling and smoothing workflow on pore shapes that deviate from spheres. This might influence the accuracy of the global correction factor. The values for the areal and volumetric correction factors, as well as the percentage of datapoints used for the linear regression are shown in Table 3.

Table 3 Data set sizes for all three parameter sets

Parameter Set	$N_{MS_{total}}$	$N_{CT_{total}}$	N_{Match}	$N_{A_{dev \leq 20\%}}$	$N_{A_{dev \leq 20\%}}/N_{Match}$	k_A	k_V
Std	682	214	210	52	25 %	0.85	0.78
GP	769	373	294	88	30 %	0.89	0.84
LoF	2494	766	670	289	43 %	0.87	0.81

The calculation of the areal and volumetric correction factors was done on matched pores, which fulfil the condition of an area difference lower than 20 %

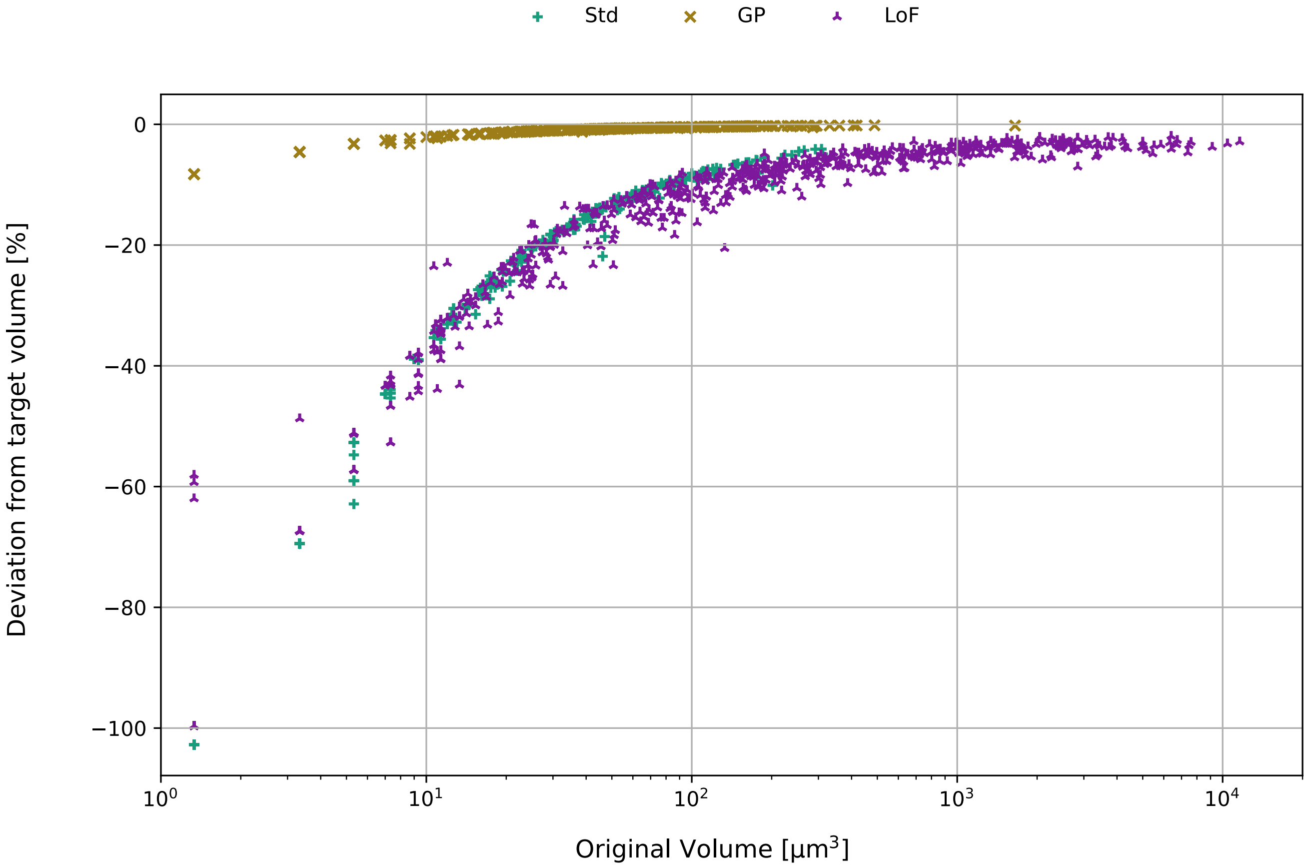

Fig. 5 Differences in volume change based on the original pore volume with a fixed rescaling factor. Due to the subdivision, the volume change does not reach the target. This effect is more pronounced for smaller pores with lower volumes ($V \leq 100$ μm^3). The scatter in volume changes for similar original volumes in the “LoF" parameter set could be explained by different sphericities of the pores and a more complex shape compared to gas pores, which influences the subdivision algorithm and the subsequent volume change

2.4 CT Data Manipulation

To reduce the systematic deviation in pore areas between both data sources, the CT data is modified. This is done by isolating each pore mesh, and then uniformly rescaling the meshes around their respective barycenters. This rescaling increases the pore volume to the target volume $V_{\mathrm{Target}} = V_{\mathrm{CT}}/k_V$. The CT pore volume is now equal to the hypothetical metallographic pore volume, which is calculated based on the pore area at the cut section with the assumption of sphericity. The pore shape however is still different due to the Marching-Cubes reconstruction of the CT data, which creates stepwise features in the pores. To reduce this stepping effect, a subdivision algorithm [21] and a smoothing algorithm [22] is used. The subdivision algorithm changes the pore shape and in turn the pore volume. A second rescaling of the mesh is therefore necessary. The rescaling factor for the second rescaling is unknown, it changes based on the pore volume. Small pores close to the resolution limit consist of fewer mesh vertices and faces, resulting in a high curvature change. The subdivision algorithm reduces the curvature changes by repositioning and adding mesh vertices. The vertex repositioning is more pronounced for pores with fewer vertices, therefore the effect on the volume change is stronger at smaller pores. An iterative algorithm is used to optimize the second rescaling factor so that the volume stays equal to the target volume. The necessity of the adaptive second rescaling factor is shown in Fig. 5. Without this second factor, the target volume change is not achieved. The effect of the subdivision algorithm on smaller pores ($V \leq 100$ μm^3) is clearly visible. The “LoF" parameter set also shows an increased scatter in the deviation to the target volume compared to the other two parameter sets. The scatter could be caused by the more complex shape of Lack-of-Fusion defects, which are often non-spherical and elongated. Images of two different pores from the datasets “GP" and “LoF" are shown in Fig. 8.

After the subdivision step, the smoothing algorithm [22] is applied. Since the smoothing algorithm used is volume conserving, the volume stays constant. The smoothing algorithm reduces the curvature, creating a more organic pore shape,

Table 4 Subdivision and smoothing parameters

Subdivision	Smoothing		
Iterations	λ	k_{PB}	N
3	0.6307	0.1	30

reducing the artefacts from the Marching-Cubes reconstruction. The parameters used for subdivision and smoothing are shown in Table 4. The subdivision and smoothing workflow is based on the article from Taubin [22], and the parameters used are explained thoroughly there.

3 Results

3.1 Volume Increase

A total number of 1174 pores were matched between both data sources in the three parameter sets. All parameter sets show a mean reduction in the area difference between both data sources, as shown in Fig. 6. The workflow and regression was applied for all matched pores, which is why the original average area deviation is larger in Fig. 6 than in Fig. 4, where only a subset of the pores is used for the regression. The size of the datasets is shown in Table 3. For the "LoF" parameter set, the area increase for pores with a cut section smaller than 5000 $\mu\mathrm{m}^2$ is larger than intended. The CT cut section area A_{CT} is larger than the metallographic cut section area A_{MS}. This is also true for the other two parameter sets, but only for a smaller cut section area of 2000 $\mu\mathrm{m}^2$ for parameter set "GP" and 500 $\mu\mathrm{m}^2$ for parameter set "Opt".

This might be caused by increasing uncertainty for pores with a small size, i. e. a low voxel count. As discussed in the introduction, CT uncertainty increases for objects close to the resolution limit [11, 13]. For pores with a cut section larger than 5000 $\mu\mathrm{m}^2$, the rescaling workflow successfully increased the cut section area to the intended size, closer to the measured area in the metallography. For all parameter sets, the absolute difference between both data sources increases with an increasing cut section area. This indicates, that the area deviation could be further reduced by using a correction factor that changes with the detected cut section

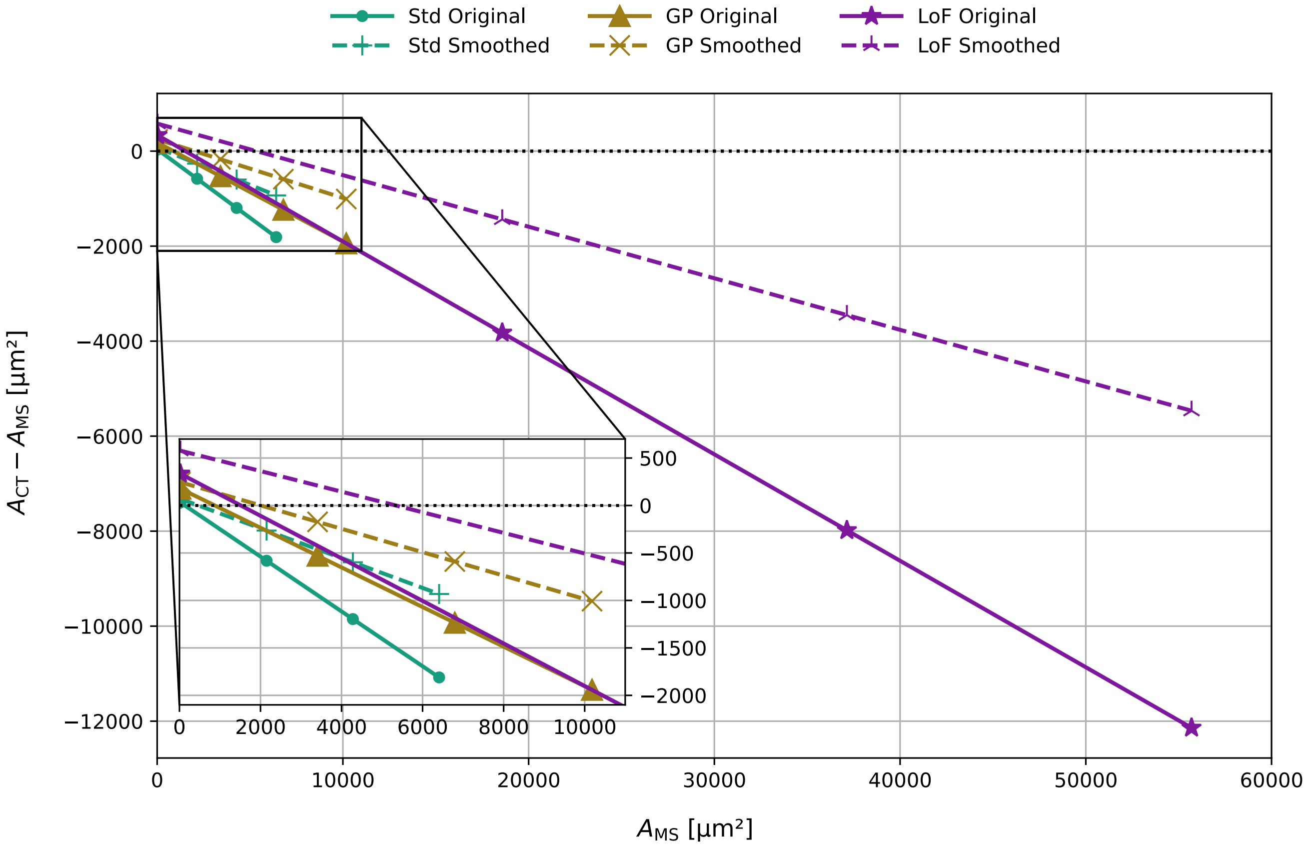

Fig. 6 The difference between linear regressions of cut section areas from microsectioning (MS) and rescaled, smoothed CT data. The workflow reduced the difference between pore areas at the cut section for all three parameter sets compared to the original CT data. The enlarged section shows a detailed view for the data sets "Std" and "GP", which have smaller cut section areas than data set "LoF"

area, and considering the parameter set “LoF" also includes the sphericity measure as a factor.

While the sphericity could be included in further datasets, a correction factor based on the size of the cut section area needs to be extracted from metallographic preparation, which is unfeasible for industrial applications, because of the destructive measure. A correlation between the cut section area and the pore volume might be useful to bypass this step.

3.2 Curvature

The effect of mesh smoothing on the pore is investigated by considering the curvature. To compare the result of the pore smoothing workflow to the initial mesh one needs to account for the mesh vertices increase by the subdivision algorithm. This is done by sorting each mesh point by curvature and a subsequent normalization of the x-axis to compare multiple pore meshes. Figure 7 shows that for all three parameter sets, the mean curvature of the smoothed meshes are lower than the mean curvature of the original meshes. To illustrate this change, Fig. 8 shows selected pores from the parameter sets “GP" and “LoF". The smoothing removes most of the stepwise features from the Marching-Cubes reconstruction, while keeping the overall shape of the pore. The red line indicates the cut-section line used for the area comparison with the metallographic image. Pores Figs. 8a and c are unsmoothed pores from the CT data, Figs. 8b and d are the pores after the rescaling and smoothing workflow. Pore Fig. 8a is extracted from the parameter set “GP" and represents a smaller pore, with a volume of $V_\mathrm{a} = 4.75 \times 10^{-5}\,\mathrm{mm}^3$ which increased 29% to $V_\mathrm{b} = 6.07 \times 10^{-5}\,\mathrm{mm}^3$ due to rescaling and smoothing. The cut section area increased by 19%. Pore Fig. 8c represents a larger pore, extracted from the parameter set “LoF", with a pore volume $V_\mathrm{c} = 6.51 \times 10^{-4}\,\mathrm{mm}^3$, increased by 24% to $V_\mathrm{d} = 8.08 \times 10^{-4}\,\mathrm{mm}^3$. The cut section area also increased by 19%.

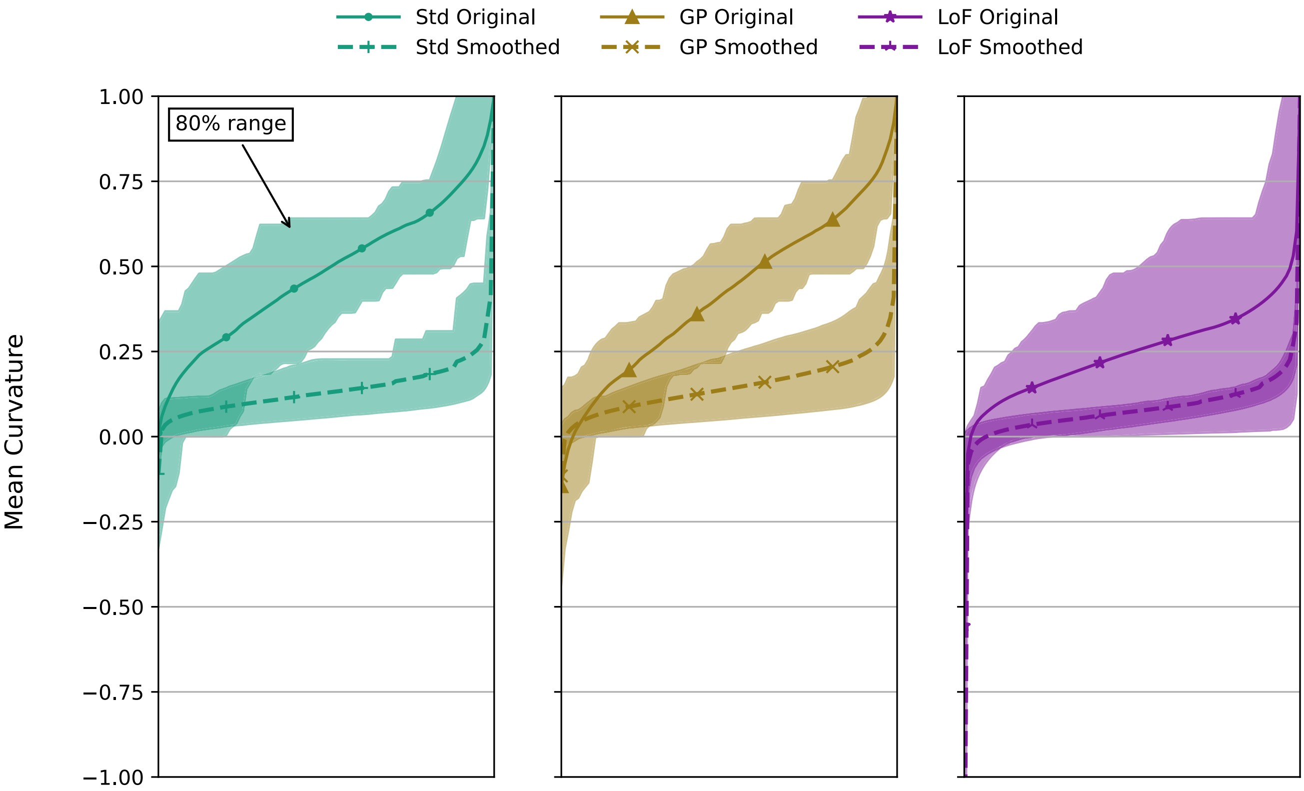

Fig. 7 Mean curvature improvement due to mesh smoothing. Thick lines show the interpolated mean values for all pores of the parameter set, while the filled area shows a range of 80% of the pore curvatures. The smoothing workflow reduces the mean curvature. The scatter of the mean curvature is also reduced, especially for the parameter set “LoF"

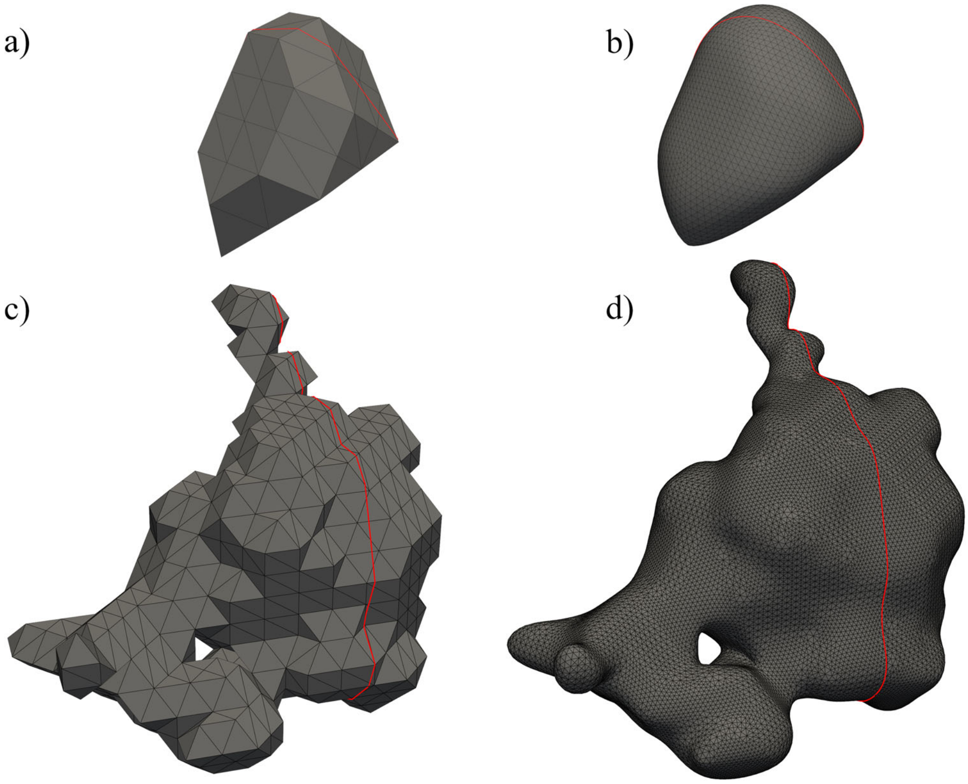

Fig. 8 Effect of the smoothing workflow on exemplary small and large pores

4 Conclusion

This study investigated the influence of data sources and data processing on the resulting pore sizes based on a dataset of 1174 pores, grouped in 3 parameter sets. A systematic reduction of cut surface areas of pores reconstructed by CT compared to pores analysed by optical imaging was discovered in all parameter sets. This underestimation of pore areas influences pore criticality estimations and leads to an underestimation of critical pores. To achieve an improved pore reconstruction, a pore rescaling, subdivision and smoothing workflow was developed. This workflow increased the pore areas at the cut surface and reduced the differences in pore area sizes from both data sources by up to 50%. For all parameter sets, the workflow produces results closer to the metallographic data compared to the original data. The mesh smoothing successfully reduced the mean curvature, as well as the scatter in mean curvatures along the mesh vertices. This improves the results of subsequent finite element simulations for pore criticality calculations, due to less pronounced mesh discretization effects and allows a more accurate pore criticality estimation.

The subdivision algorithm increases the number of mesh vertices, which increases data size. For further processing, the number of mesh vertices might need to be reduced, to allow for feasible computation times. A balance between processability and mesh accuracy needs to be found. This could be achieved with a mesh vertex reduction scheme, which would change the pore shape again.

The rescaling factors are based on a global linear regression, which does not consider outliers. A deeper investigation into the sources of these outliers could help in developing better rescaling factors. The rescaling factors were developed on datasets which show an increased amount of specific defects (Lack-of-Fusion defects or Gas Pores). However, there is no defect exclusivity in the pore datasets, gas porosity also exists in the “LoF" dataset, which could influence the result of the regression and in turn the rescaling factor. This could be alleviated by an a-priori classification of the defects, as was done in [12]. A pore size specific correction might capture the increasing uncertainty for defect sizes closer to the resolution limit.

The mechanical preparation of the metallographic images might also introduce preparation-induced errors that alter the shape and size of the defects. The impact of this error source was not considered.

Further research needs to be done to accurately assess the influence of the CT scan parameters on the dimensional accuracy. The results of this article are rooted in the scanning parameters that were used. Applicability to other parameter sets need further validation. This research also needs to include the unique issues of AM, e.g. loose powder in Lack-of-Fusion defects influences the pore density, potentially different behaviour of various powder materials. Further exploration of parameter-dependent correction factors and non-spherical pores will help refine pore assessments, particularly for complex defect morphologies. Further work on porosity generated by CT data needs to acknowledge the various error sources and use the aforementioned workflow or other mentioned options to reduce the dimensional error and decrease the uncertainty. Since the pore size is crucial for fatigue assessments and AM quality assurance, the reduction of dimensional errors in CT scans should be a research target. For the specific purpose of pore criticality estimation, the largest pores are of importance and should therefore also be the focus for studies on the dimensional accuracy.

Author Contributions The authors confirm contribution to the paper as follows: study conception and design: S.M., M.B., D.H.; data collection: S.M., M.B.; analysis and interpretation of results: S.M.; draft manuscript preparation: S.M.; draft review and editing: D.H., I.K.; All authors reviewed the manuscript.

Funding Open Access funding enabled and organized by Projekt DEAL. The work described is financed with funds from the German Federal Ministry of Education and Research (BMBF) under Reference No: 01LY2113C

Data Availability Data is available on reasonable request.

Declarations

Competing Interest The authors declare no competing interests.

References

1. Sanaei, N., Fatemi, A., Phan, N.: Defect characteristics and analysis of their variability in metal l-pbf additive manufacturing. Mater. Des. **182**, 108091 (2019). https://doi.org/10.1016/j.matdes.2019.108091
2. Mostafaei, A., Zhao, C., He, Y., Reza Ghiaasiaan, S., Shi, B., Shao, S., Shamsaei, N., Wu, Z., Kouraytem, N., Sun, T., Pauza, J., Gordon, J.V., Webler, B., Parab, N.D., Asherloo, M., Guo, Q., Chen, L., Rollett, A.D.: Defects and anomalies in powder bed fusion metal additive manufacturing. Curr. Opin. Solid State Mater. Sci. **26**(2), 100974 (2022). https://doi.org/10.1016/j.cossms.2021.100974
3. Murakami, Y.: Metal Fatigue, 2nd edn. Elsevier Science & Technology, Chantilly (2019). https://doi.org/10.1016/C2016-0-05272-5
4. Romano, S., Abel, A., Gumpinger, J., Brandão, A.D., Beretta, S.: Quality control of alsi10mg produced by slm: Metallography versus ct scans for critical defect size assessment. Addit. Manuf. **28**, 394–405 (2019). https://doi.org/10.1016/j.addma.2019.05.017
5. Dezecot, S., Maurel, V., Buffiere, J.-Y., Szmytka, F., Koster, A.: 3d characterization and modeling of low cycle fatigue damage mechanisms at high temperature in a cast aluminum alloy. Acta Mater. **123**, 24–34 (2017). https://doi.org/10.1016/j.actamat.2016.10.028
6. Le, V.-D., Saintier, N., Morel, F., Bellett, D., Osmond, P.: Investigation of the effect of porosity on the high cycle fatigue behaviour of cast al-si alloy by x-ray micro-tomography. Int. J. Fatigue. **106**, 24–37 (2018). https://doi.org/10.1016/j.ijfatigue.2017.09.012
7. Awd, M., Labanie, M.F., Moehring, K., Fatemi, A., Walther, F.: Towards deterministic computation of internal stresses in additively manufactured materials under fatigue loading: Part i. Materials (Basel, Switzerland). **13**(10) (2020). https://doi.org/10.3390/ma13102318
8. Tammas-Williams, S., Withers, P.J., Todd, I., Prangnell, P.B.: The influence of porosity on fatigue crack initiation in additively manufactured titanium components. Sci. Rep. **7**(1), 7308 (2017). https://doi.org/10.1038/s41598-017-06504-5
9. Evans, L.M., Sözümert, E., Keenan, B.E., Wood, C.E., Du Plessis, A.: A review of image-based simulation applications in high-value manufacturing. Arch. Computat. Methods Eng. State Art. Rev. **30**(3), 1495–1552 (2023). https://doi.org/10.1007/s11831-022-09836-2
10. Du Plessis, A., Le Roux, S.G., Els, J., Booysen, G., Blaine, D.C.: Application of microct to the non-destructive testing of an additive manufactured titanium component. Case Stud. Nondestruct. Test. Eval. **4**, 1–7 (2015). https://doi.org/10.1016/j.csndt.2015.09.001
11. Villarraga-Gómez, H., Thousand, J.D., Smith, S.T.: Empirical approaches to uncertainty analysis of x-ray computed tomography measurements: A review with examples. Precis. Eng. **64**, 249–268 (2020). https://doi.org/10.1016/j.precisioneng.2020.03.004
12. Holgado, I., Ortega, N., Yagüe-Fabra, J.A., Plaza, S., Villarraga-Gómez, H.: Metrological evaluation and classification of porosity in metal additive manufacturing using x-ray computed tomography. Mater. Des. **254**, 114057 (2025). https://doi.org/10.1016/j.matdes.2025.114057
13. Carmignato, S., Pierobon, A., Rampazzo, P., Parisatto, M., Savio, E., *et al.*: Ct for industrial metrology-accuracy and structural resolution of ct dimensional measurements. In: 4th Conference on Industrial Computed Tomography (iCT), pp. 19–21 (2012)
14. Dewulf, W., Kiekens, K., Tan, Y., Welkenhuyzen, F., Kruth, J.-P.: Uncertainty determination and quantification for dimensional measurements with industrial computed tomography. CIRP Ann. **62**(1), 535–538 (2013). https://doi.org/10.1016/j.cirp.2013.03.017
15. Schild, L., Weiser, L., Höger, K., Lanza, G.: Analyzing the error of computed tomography-based pore detection by using microscope images of matched cross-sections. Precis. Eng. **81**, 192–206 (2023). https://doi.org/10.1016/j.precisioneng.2023.01.013
16. Lifton, J., Liu, T.: An adaptive thresholding algorithm for porosity measurement of additively manufactured metal test samples via x-ray computed tomography. Addit. Manuf. **39**, 101899 (2021). https://doi.org/10.1016/j.addma.2021.101899
17. Otsu, N.: A threshold selection method from gray-level histograms. IEEE Trans. Syst. Man Cybern. **9**(1), 62–66 (1979). https://doi.org/10.1109/TSMC.1979.4310076
18. Thomas Lewiner, A.W.V. Hélio Lopes, Tavares, G.: Efficient implementation of marching cubes' cases with topological guarantees. J. Graph. Tools. **8**(2), 1–15 (2003). https://doi.org/10.1080/10867651.2003.10487582

19. Walt, S., Schönberger, J.L., Nunez-Iglesias, J., Boulogne, F., Warner, J.D., Yager, N., Gouillart, E., Yu, T., contributors: scikit-image: image processing in Python. PeerJ. **2**, 453 (2014). https://doi.org/10.7717/peerj.453
20. Pedregosa, F., Varoquaux, G., Gramfort, A., Michel, V., Thirion, B., Grisel, O., Blondel, M., Prettenhofer, P., Weiss, R., Dubourg, V., et al.: Scikit-learn: Machine learning in python. J. Mach. Learn. Res. **12**, 2825–2830 (2011)
21. Barthe, L., Kobbelt, L.: Subdivision scheme tuning around extraordinary vertices. Comput. Aided Geom. Des. **21**(6), 561–583 (2004). https://doi.org/10.1016/j.cagd.2004.04.003
22. Taubin, G.: A signal processing approach to fair surface design. In: Proceedings of the 22nd Annual Conference on Computer Graphics and Interactive Techniques. SIGGRAPH ’95, pp. 351–358. Association for computing machinery, New York, NY, USA (1995). https://doi.org/10.1145/218380.218473